Dalton Transactions

PAPER

View Article Online
View Journal | View Issue

Cite this: *Dalton Trans.*, 2014, **43**, 16105

Synthesis of novel and stable g-C_3N_4/N-doped $SrTiO_3$ hybrid nanocomposites with improved photocurrent and photocatalytic activity under visible light irradiation†

Santosh Kumar,[a] Surendar Tonda,[a] Arabinda Baruah,[b] Bharat Kumar[b] and Vishnu Shanker*[a]

Received 11th April 2014,
Accepted 26th August 2014

DOI: 10.1039/c4dt01076k

www.rsc.org/dalton

Hybrid nanocomposites based on N-doped $SrTiO_3$ nanoparticles wrapped in g-C_3N_4 nanosheets were successfully prepared by a facile and reproducible polymeric citrate and thermal exfoliation method. The results clearly indicated that the N-doped $SrTiO_3$ nanoparticles are successfully wrapped in layers of the g-C_3N_4 nanosheets. The g-C_3N_4/N-doped $SrTiO_3$ nanocomposites showed absorption edges at longer wavelengths compared with the pure g-C_3N_4 as well as N-doped $SrTiO_3$. The hybrid nanocomposites exhibit an improved photocurrent response and photocatalytic activity under visible light irradiation. Interestingly, the hybrid nanocomposite possesses high photostability and reusability. Based on experimental results, the possible mechanism for prolonged lifetime of the photoinduced charge carrier was also discussed. The high performance of the g-C_3N_4/N-doped $SrTiO_3$ photocatalysts is due to the synergic effect at the interface of g-C_3N_4 and N-doped $SrTiO_3$ hetero/nanojunction including the high separation efficiency of the charge carrier, band energy matching and the suppressed recombination rate. Therefore, the hybrid photocatalyst could be of potential interest for water splitting and environmental remediation under natural sunlight.

1. Introduction

Photocatalysis technology can mimic natural photosynthesis to directly convert solar energy into chemical energy, and represents an attractive strategy for clean energy production and environmental remediation.[1,2] However, this technology has been widely investigated for hydrogen production from water splitting, solar cells and the degradation of organic pollutants in water or air without leaving behind any hazardous residues.[1–5] Unfortunately, most of the widely employed semiconductor photocatalysts are active only under UV-light irradiation.[6–9] Since the solar spectrum consists of only 4–5% of UV-light, visible light photocatalysis could be highly economical from a practical application point of view.[10] In the past few decades, tremendous efforts have been made for improving photocatalytic efficiency under visible light irradiation.[10–13] Recently, the 2D graphitic carbon nitride (g-C_3N_4) nanosheet, a typical metal-free polymeric semiconductor material, has attracted a great deal of scientific interest due to its suitable band gap to absorb the visible light and unique properties including high chemical and structure stability, high redox ability, high surface area and low cost.[14,15] However, the efficiency of the g-C_3N_4 is still limited, due to the poor visible light response, high recombination rate and low separation efficiency of photoinduced electron–hole pairs.

On other hand, perovskite structure $SrTiO_3$ has attracted considerable attention in photocatalysis technology due to its interesting physical, chemical and structural properties.[16–18] Moreover, $SrTiO_3$ has favourable band edge potentials and delocalized nature of photoexcited electrons which are the primary reasons for its higher efficiency. However, the intrinsic large bandgap energy (E_g = 3.2 eV) of $SrTiO_3$ allows only the utilization of the UV region.[19] A large number of metals and non-metals have been doped into the crystal structure of $SrTiO_3$ to alter its electronic bandgap for visible light response.[20–24] Unfortunately, metal doping can also create phase impurity which can serve as a recombination centre for photoinduced electron–hole pairs. Non-metal doping (namely N-doping) into the crystal structure of $SrTiO_3$ provides an

[a]*Department of Chemistry, National Institute of Technology, Warangal-506004, A.P., India. E-mail: vishnu@nitw.ac.in; Fax: +91-870-2459547; Tel: +91-870-2462675*
[b]*Department of Chemistry, Indian Institute of Technology Delhi, New Delhi-110016, India*

†Electronic supplementary information (ESI) available. See DOI: 10.1039/c4dt01076k

alternative strategy to bring photocatalytic activity under visible light irradiation.[25] However, the efficiency is not enough for its potential applications in photocatalytic environmental remediation. Therefore, the strategies for making the $SrTiO_3$ a valuable visible light active photocatalyst have been continuously pursued.

The formation of heterostructure by direct coupling of two semiconductors is an effective approach to promote separation of charge carriers for improved photocatalytic activity.[26–28] The type-II (staggered bandgap) heterostructure has the obvious merit of forming a favourable interface combination, and the energy gradient existing at the interfaces tends to spatially separate charge carriers on different sides of the hetero/nano-junction in which electrons can be confined to one side and holes to the other side.[12] The spatially localized electrons and holes in the type-II hetero/nano-structures could make them more suitable candidates for improved photocatalysis. The g-C_3N_4/$SrTiO_3$ hybrid composite is typical of type-II heterostructures. X. Xu *et al.* reported a synthesis of g-C_3N_4 coated $SrTiO_3$ as a photocatalyst for the photocatalytic evolution of H_2. H. W. Kang *et al.* also reported that the g-C_3N_4/$SrTiO_3$:Rh heterojunction showed an enhanced photoactivity for H_2 evolution when compared with g-C_3N_4 as well as $SrTiO_3$. These reports mainly focused on the preparation of the g-C_3N_4/$SrTiO_3$ heterojunction and photocatalytic activity for H_2 evolution.[29,30] It is also important to promote the direct Z-scheme charge carrier transfer process by creating a favorable interface in the heterostructure.[31] Since the evaluation of potential photocatalytic Z-schemes is of critical importance given the growing need for an efficient and inexpensive means of harnessing the huge energy potential of solar irradiation to renewable hydrogen energy from water splitting and the degradation of organic pollutants.[32–34]

In this work, novel g-C_3N_4/N-doped $SrTiO_3$ hybrid nanocomposites have been synthesized by a facile and reproducible polymeric citrate and thermal exfoliation method. The g-C_3N_4/N-doped $SrTiO_3$ organic–inorganic hybrid nanocomposites were characterised by powder X-ray diffraction (XRD), thermogravimetric analysis (TGA), UV–Vis diffuse reflectance spectroscopy (UV-Vis DRS), Fourier transform infrared spectroscopy (FTIR), transmission electron microscopy (TEM), X-ray photoelectron spectroscopy (XPS), electrochemical impendence spectroscopy (EIS) and photoluminescence (PL). The results demonstrated that after hybridization of g-C_3N_4 with N-doped $SrTiO_3$, enhanced photocurrent response and photocatalytic activity was achieved under visible light irradiation due to the prolonged lifetime of the photoinduced charge carrier. The synergic effect at the interface of g-C_3N_4 and N-doped $SrTiO_3$ nanojunction and the possible Z-scheme mechanism of prolonged lifetime of the photoinduced charge carrier were also discussed. Therefore, the hetero/nano-structured photocatalyst could be of potential interest for water splitting as well as environmental remediation under natural sunlight. However, to the best of our knowledge there has been no report on the synthesis of the g-C_3N_4/N-doped $SrTiO_3$ hybrid nanocomposite photocatalysts.

2. Experimental details

2.1 Materials

Melamine (Aldrich, 99.0%), strontium nitrate (Aldrich, 99.0%), titanium isopropoxide (Aldrich, 99.7% metal based) (Qualigens, LR grade, 99.5%), citric acid (Qualigens, AR grade, 99.5%) and rhodamine B (Aldrich, 85.0%) were used as received. All other reagents used in this work were analytically pure and were used without further purification.

2.2 Method

2.2.1 Preparation of g-C_3N_4 nanosheets. The nanosheets were prepared by thermal exfoliation of the bulk g-C_3N_4.[15] In brief, 0.5 g of the bulk g-C_3N_4 was placed in an open ceramic boat and was heated at 500 °C for 2 h with a ramp rate of 5 °C min^{-1} and named CN. The bulk g-C_3N_4 was prepared according to an earlier report.[28]

2.2.2 Preparation of N-doped $SrTiO_3$ nanoparticles. First, 0.1 M aqueous solution of Ti^{4+} was prepared by adding 1 mL of titanium isopropoxide to 5.9 mL of ethylene glycol and 5.5 g of citric acid under a nitrogen atmosphere (avoid hydrolysis of moisture sensitive titanium isopropoxide) to form a water soluble titanium-citrate complex at room temperature. To this solution, appropriate amounts of strontium nitrate and glycine (N source) were added and stirred for 2 h at room temperature. Further the mixture (sol) was aged to form a viscous gel. The resulting gel was subjected to charring at 350 °C for 4 h. The black powder obtained was then calcined at 550 °C for 8 h to prepare pure N-doped $SrTiO_3$ nanoparticles and was named STON. The pure $SrTiO_3$ nanoparticles were prepared in the absence of N source under the same experimental conditions and was named STO.

2.2.3 Preparation of g-C_3N_4/N-doped $SrTiO_3$ hybrid nanocomposites. The preparation of g-C_3N_4/N-doped $SrTiO_3$ nanocomposites was done as follows: in brief, an appropriate amount of N-doped $SrTiO_3$ powder was mixed and ground well with 0.5 g of bulk g-C_3N_4 and then calcined at 500 °C for 2 h under static air. The hybrid nanocomposites with 5 wt%, 10 wt %, 15 wt% and 20 wt% of N-doped $SrTiO_3$ are named CNSTON5, CNSTON10, CNSTON15, and CNSTON20, respectively.

2.3 Characterization

X-ray diffraction studies (XRD) were performed on a Bruker D8 Advance diffractometer using Ni filtered Cu Kα radiation. Thermogravimetric analysis (TGA) was done on a PerkinElmer Pyris Diamond TGA/DTA system on well ground samples under air atmosphere with a heating rate of 10 °C min^{-1}. The Fourier transform infrared (FTIR) spectra were recorded in transmission mode from 4000 to 400 cm^{-1} on a Nicolate Protégé 460 FTIR spectrometer using KBr discs. Transmission electron microscopy (TEM) was done on a JEOL, JSM-6700F instrument. Chemical compositions of the prepared samples were analysed by X-ray photoelectron spectroscopy (Kratos Axis ULTRA incorporating a 165 mm hemispherical electron energy analyzer). UV-Vis diffuse reflectance spectra were recorded on

a Lambda/20 Instrument (UV-Vis NIR spectrophotometer), equipped with an integrating sphere to record the diffuse reflectance spectra of the prepared samples, and $BaSO_4$ was used as a reference. The photoluminescence (PL) studies were carried out on TSC solutions using an F96PRO fluorescence spectrophotometer with an excitation wavelength of 365 nm.

2.4 Photocatalytic activity

Rhodamine B (RhB), a widely used and stable dye, was selected as a colored model pollutant and 4-chlorophenol as a colorless model pollutant. The photocatalytic activity of the prepared samples (0.05 g) was evaluated for the degradation of RhB and 4-chlorophenol aqueous solution (100 mL, 5 mg L^{-1}) under visible light irradiation. The visible light source for the photo-irradiation is a solar simulator 300 W Xe lamp (Asahi Spectra Co., Ltd) with a supercold filter, which provides the visible light region ranging from 400 nm to 700 nm and a light intensity of 115 mW cm^{-2}. Prior to irradiation, the aqueous solution was suspended with a catalyst and stirred under dark conditions for 30 min to ensure that the surface of the catalyst was saturated with RhB molecules. During photocatalytic processes, the sample was periodically withdrawn, centrifuged to separate the catalyst from the aqueous solution, and used for the absorbance measurements. The absorption spectra were recorded on a UV–Vis spectrophotometer.

2.5 Detection of reactive species

The reactive species detection process is very similar to the photocatalytic degradation process. Different scavengers were added into the RhB aqueous solution prior to addition of a catalyst. Photoluminescence (PL) spectra with terephthalic acid (TA) as a probe molecule were used to confirm the formation of $^{\bullet}OH$ on the catalyst surface under visible light irradiation.[35] In a brief experimental procedure, the catalyst (0.05 g) was dispersed in 40 mL of the TA (5×10^{-4} mol L^{-1}) aqueous solution with NaOH (2×10^{-3} mol L^{-1}) at room temperature. The above suspension was irradiated to evaluate the photocatalytic activity of the catalyst and the sample was periodically withdrawn, centrifuged to separate the catalyst from the aqueous solution, and used for the PL measurements.

2.6 Electrochemical impedance and photocurrent measurements

Electrochemical impedance and photocurrent measurements were done on an electrochemical workstation (ZAHNER IM6e Electrik, Germany) based on a conventional three-electrode system comprised of indium-tin oxide (ITO) coated with a catalyst as the working electrode, a platinum wire as the counter electrode, and Ag/AgCl (3 N KCl) as the reference electrode. The EIS experiments were carried out in a 0.1 M Na_2SO_4 solution containing 5 mM $[Fe(CN)_6]^{3-}/[Fe(CN)_6]^{4-}$ with a frequency range from 0.01 Hz to 100 kHz at 0.24 V, and the amplitude of the applied sine wave potential in each case was 5 mV. The transient photocurrent responses of the pure samples were investigated for several on–off cycles of irradiation by a Xe lamp through a UV-cutoff filter. 0.01 M Na_2SO_4 aqueous solution was used as the electrolyte. The working electrodes were prepared by a simple method as follows: 5 mg of the sample was dispersed in 1 mL double distilled water to make slurry. The slurry (20 μL) was then dripped on the ITO glass with a 1 cm × 0.5 cm area and dried at 120 °C for 1 h.

3. Results and discussion

3.1 Catalyst characterization

The contents of N-doped $SrTiO_3$ wrapped into the layers of g-C_3N_4 nanosheets were successfully determined by thermogravimetric analysis (TGA) under air atmosphere from 50 to 800 °C with a heating rate of 10° min^{-1}. The decomposition of g-C_3N_4 starts at 540 °C and is complete at ~710 °C which is attributed to the burning of g-C_3N_4 as shown in Fig. 1.[14] In all g-C_3N_4/N-doped $SrTiO_3$ hybrid nanocomposites, this particular weight loss region was observed and the g-C_3N_4 content was easily determined from the corresponding weight loss in the thermogram (TG). The weight percentages of N-doped $SrTiO_3$ loaded were found to be 5.1, 10.1 15.2, and 20.2 for CNSTON5, CNSTON10, CNSTON15 and CNSTON20, respectively. These contents were nearly consistent with the dosage of N-doped $SrTiO_3$ loaded in the hybrid nanocomposites.

Fig. 2 shows the XRD patterns of the g-C_3N_4 nanosheet, $SrTiO_3$, N-doped $SrTiO_3$ nanoparticles and g-C_3N_4/N-doped $SrTiO_3$ hybrid nanocomposites. The diffraction peaks of the pure $SrTiO_3$ and N-doped $SrTiO_3$ are well indexed as the cubic phase of $SrTiO_3$ (JCPDS #894934). The diffraction peaks of N-doped $SrTiO_3$ were broader with low intensity and their positions are located at slightly higher angle than that of pure $SrTiO_3$ (Fig. S1†), indicating the decrease in crystallinity and an overall contraction of the lattice parameters due to successful incorporation of N into the $SrTiO_3$ lattice.[35] For the g-C_3N_4 nanosheet, a strong characteristic peak at 2θ = 27.5° corresponding to the characteristic interplanar stacking peak (002) of the aromatic system was clearly seen.[14] The characteristic

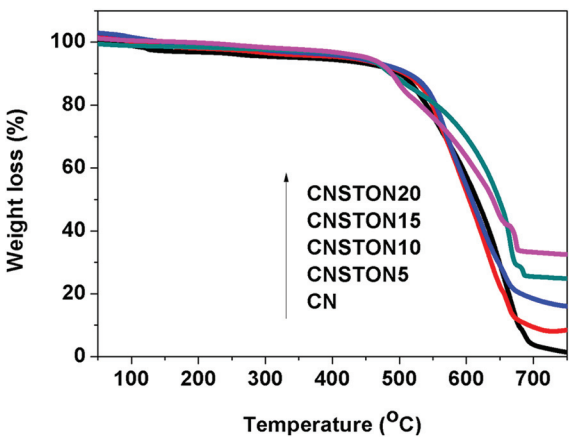

Fig. 1 TGA curves for the g-C_3N_4 nanosheet and g-C_3N_4/N-doped $SrTiO_3$ hybrid nanocomposites.

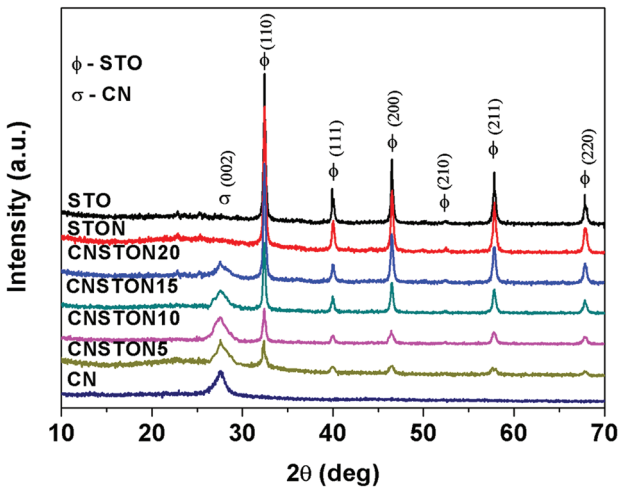

Fig. 2 The XRD patterns of the prepared photocatalysts.

peaks of g-C_3N_4 and cubic phase of N-doped $SrTiO_3$ were also present in g-C_3N_4/N-doped $SrTiO_3$ hybrid nanocomposites, indicating that the crystal structure of N-doped $SrTiO_3$ did not change after hybridization with g-C_3N_4. Moreover, no other impurity phase was seen, indicating that the g-C_3N_4/N-doped $SrTiO_3$ is a two phase composite.

Fig. 3a shows the FTIR spectra of the g-C_3N_4 nanosheet, N-doped $SrTiO_3$ and g-C_3N_4/N-doped $SrTiO_3$ hybrid nanocomposites. For N-doped $SrTiO_3$, a strong signal at 1460 cm^{-1} corresponds to the interstitial N–O species.[36,37] Moreover, the broad band in the region from 500 to 700 cm^{-1} corresponds to the Ti–O stretching vibrations.[38] For g-C_3N_4, the broad band at around 3100 cm^{-1} corresponds to the N–H stretching vibration, and the peaks at 1243 cm^{-1} and 1637 cm^{-1} correspond to C–N and C=N stretching vibrations, respectively.[27] The characteristic peak of g-C_3N_4 at 808 cm^{-1} corresponds to the s-triazine ring vibrations.[39] The characteristic bands of g-C_3N_4 and N-doped $SrTiO_3$ were present in the g-C_3N_4/N-doped $SrTiO_3$ hybrid nanocomposites.

Fig. 3b shows the UV-Vis diffuse reflectance spectra of the prepared samples. The g-C_3N_4 nanosheets exhibit a strong absorption edge in the visible region. Compared to the $SrTiO_3$, the N-doped $SrTiO_3$ shows a red shift in absorption wavelength which supports the successful incorporation of N into the $SrTiO_3$ lattice. The g-C_3N_4/N-doped $SrTiO_3$ hybrid nanocomposites also showed a red shift in absorption wavelength compared to the pure g-C_3N_4 and N-doped $SrTiO_3$. This might be due to the strong interaction between N-doped $SrTiO_3$ and g-C_3N_4 in the hetero/nanojunction. The band gap energies of the CN, STO, and STON photocatalysts were estimated using the Kubelka–Munk function to be 2.72, 3.25 and 3.02, respectively.[40]

The morphology and nanostructures of the synthesized samples were investigated by TEM. Fig. 4a shows the TEM image of the g-C_3N_4 nanosheet, indicating that g-C_3N_4 has the typical two-dimensional sheet with layered structure. Fig. 4b shows the TEM image of CNSTON15 nanocomposites. It can be seen that N-doped $SrTiO_3$ nanoparticles are successfully wrapped into the layers. The $SrTiO_3$ nanoparticles mainly exhibit a cube-like shape and have an average particle size of 50 nm as shown in Fig. S2.† Fig. 5a shows the magnified TEM image of CNSTON15, which indicates that the surfaces of $SrTiO_3$ were wrapped with g-C_3N_4 nanosheets. Fig. 5b shows the HRTEM image of CNSTON15, in which the observed lattice spacing of 0.276 nm and 0.325 nm corresponds to the (110) plane of $SrTiO_3$ and the (002) plane of g-C_3N_4, respectively.[29,41] Therefore, the TEM and HR-TEM studies confirm the formation of heterojunctions in a g-C_3N_4/N-doped $SrTiO_3$ system.

The surface compositions of the N-doped $SrTiO_3$ nanoparticles and the g-C_3N_4/N-doped $SrTiO_3$ hybrid nanocomposite were examined by X-ray photoelectron spectroscopy (XPS). Fig. 6a shows the XPS of N 1s. The observed peaks at 395.5, 396.3, 397.8 and 399.2 eV correspond to substituted N-species in different chemical environments, such as Ti–N, O–Ti–N, Ti–N–O and N–O bonds.[20,22,42] Fig. 6b shows the detailed XPS of Ti 2p for STO, STON and CNSTON15. The XPS for Ti shows two peaks of Ti $2p_{3/2}$ and Ti $2p_{1/2}$.[29] The binding energies of the Ti $2p_{3/2}$ (457.5 eV) and Ti $2p_{1/2}$ (463.1 eV) for

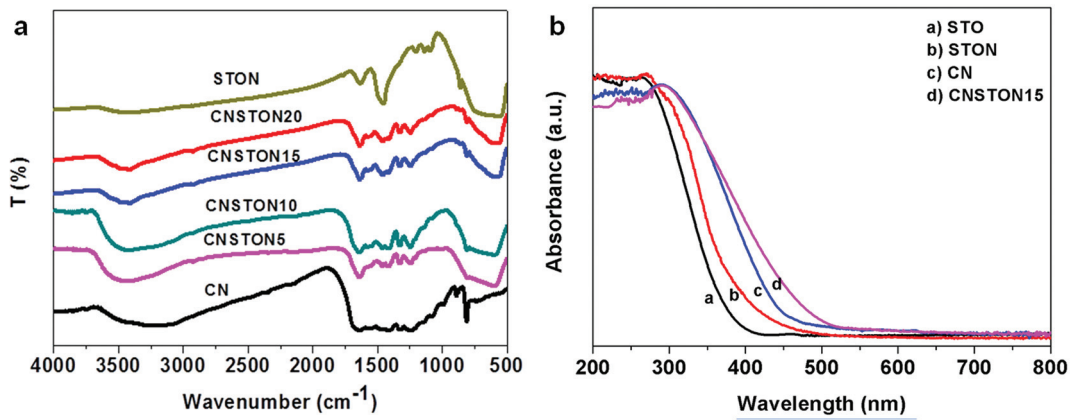

Fig. 3 FTIR (a) and UV-Vis DRS (b) spectra of the prepared photocatalysts.

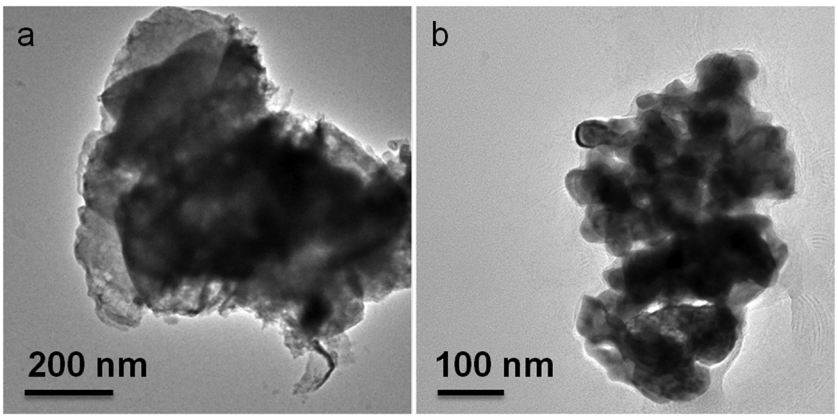

Fig. 4 TEM images of the prepared CN (a) and CNSTON15 (b) photocatalysts.

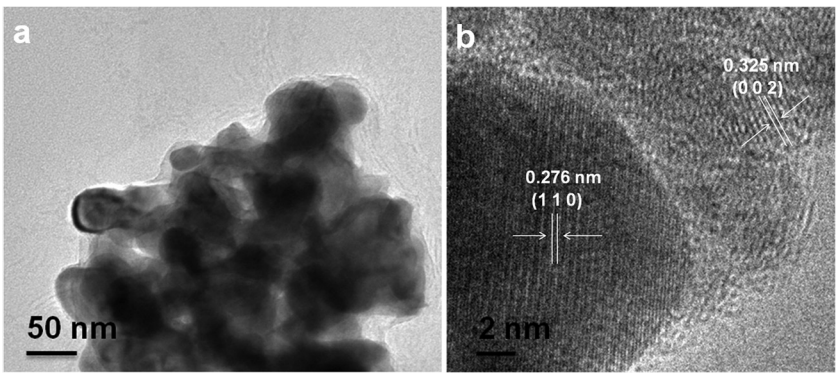

Fig. 5 Magnified TEM image (a) and HR-TEM image (b) of CNSTON15.

STON are lower than those of Ti $2p_{3/2}$ (458.1 eV) and Ti $2p_{1/2}$ (464.0 eV) for pure STO. The red shift in the binding energy of Ti 2p is due to the N-doping which can reduce Ti^{4+} to Ti^{3+}.[43] Additionally, the typical lines for Ti $2p_{1/2}$ (464.4 eV) and Ti $2p_{3/2}$ (458.2 eV) are clearly resolved for N-doped $SrTiO_3$ while for the CNSTON15 nanocomposite these lines are entirely undetectable. The shift of Ti–N bonds was induced by the formation of oxygen vacancies (O_{vac}) and the Ti^{3+} cations adjacent to the vacancies.[20] The g-C_3N_4 normally shows a characteristic C 1s line at about 288.1 eV along with the adventitious C 1s (284.6 eV), which corresponds to the carbon (C/N–C) as shown in Fig. 6c.[29] This line was found to be slightly shifted to a lower energy (287.8 eV) for the CNSTON15 due to charge transfer between N-doped $SrTiO_3$ and g-C_3N_4 in the heterostructure. The XPS results are consistent with the results of TEM that the N-doped $SrTiO_3$ surface was wrapped by the g-C_3N_4. Therefore, the XPS spectra of composites contain only surface information as it is a surface technique.

3.2 Photocatalytic performance

Fig. 7a shows the photocatalytic activity of the prepared samples for degradation of RhB under visible light irradiation. The g-C_3N_4/N-doped $SrTiO_3$ hybrid photocatalysts exhibited significantly higher photocatalytic activity than that of pure g-C_3N_4 and N-doped $SrTiO_3$. It was observed that the efficiency of photolysis (absence of catalyst) is negligible under the same experimental conditions, which indicates that RhB is stable under visible light irradiation (Fig. S3†). Moreover, the adsorption ability of the g-C_3N_4 nanosheet and g-C_3N_4/N-doped $SrTiO_3$ hybrid photocatalysts was also investigated under the dark conditions for the same duration (Fig. S4†). The adsorption ability of these photocatalysts is almost the same, which indicates that the photoinduced charge separation might be playing a major role in the enhancement of photocatalytic efficiency. The results also indicate that both light and catalyst are necessary for the effective photocatalytic degradation of RhB under visible light irradiation. The experimental photocatalytic data were highly fitted in the pseudo first-order kinetic equation $\ln(C/C_0) = -kt$ as shown in Fig. 7b. The apparent rate constants estimated were 0.0113 min^{-1}, 0.0038 min^{-1}, 0.0135 min^{-1} and 0.0558 min^{-1} for CN, STO, STON and CNSTON15, respectively. It is clearly observed that the photocatalytic activity of CNSTON15 is almost 5 times higher than that of CN and 4 times higher than that of STON.

Moreover, the photocatalytic activity of the prepared samples was also evaluated for degradation of 4-chlorophenol (chosen as a colorless model organic pollutant) under visible light irradiation as shown in Fig. S5.† It can be seen that the efficiency of photolysis was negligible under the same experimental conditions, which indicates that the 4-chlorophenol is

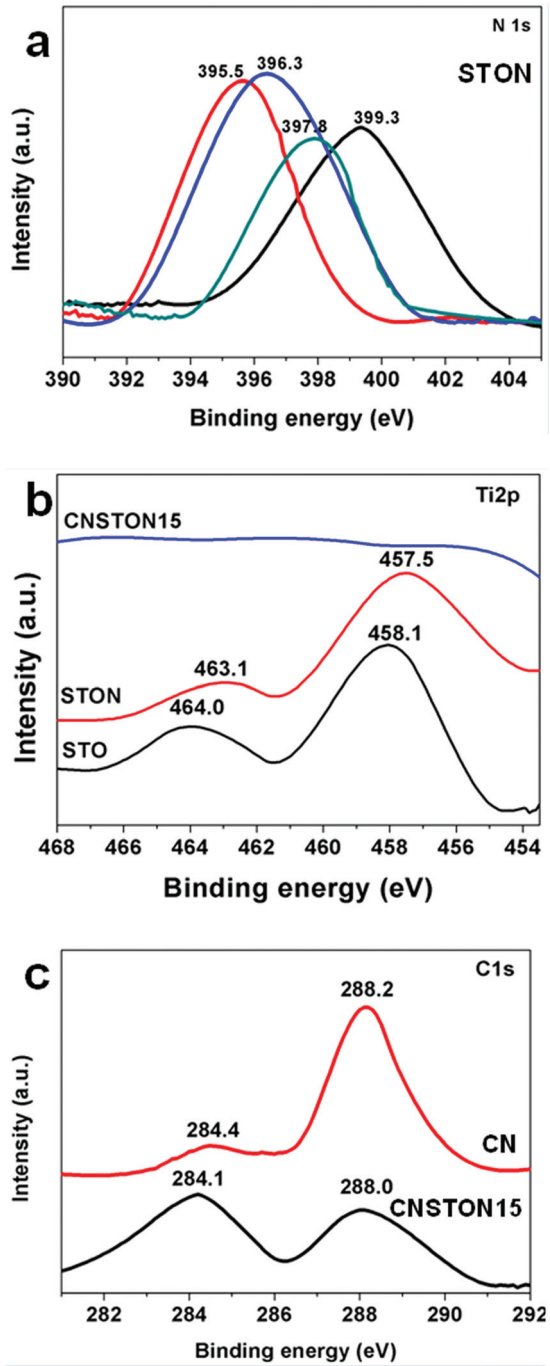

Fig. 6 XPS of the prepared photocatalysts: (a) N 1s, (b) Ti 2p and (c) C 1s.

stable under visible light irradiation. More attractively, the optimum photocatalytic activity of CNSTON15 for the degradation of 4-chlorophenol is much higher than that of the pure g-C_3N_4 and N-doped $SrTiO_3$, indicating that the g-C_3N_4/N-doped $SrTiO_3$ composite was an efficient visible light photocatalyst not only for colored pollutants but also for colorless pollutants. The photocatalytic performance reveals that these hybrid nanocomposites could be a promising photocatalyst for degradation of organic pollutants under natural sunlight.

3.3 Photoluminescence

It is well known that the photoluminescence emission spectra result from the recombination of free carriers.[44] In order to determine the role of photoinduced electron–hole pairs in the prepared samples, the photoluminescence studies were investigated. Fig. 8a shows the PL spectra of g-C_3N_4 and g-C_3N_4/N-doped $SrTiO_3$ photocatalysts with an excitation wavelength of 365 nm at room temperature. It can be seen that the pure g-C_3N_4 has a strong emission peak at about 460 nm. After hybridisation with N-doped $SrTiO_3$, the intensity of the emission peak greatly decreases, suggesting that the recombination rate of photoinduced electron–hole pairs in hybrid composites is greatly suppressed.[41] The result means that lower photoluminescence intensity indicates a higher photocatalytic activity.

3.4 Electrochemical impedance

EIS measurement was performed for CN and CNSTON15 to disclose the charge transfer resistance and the separation efficiency of the photoinduced electron–hole pairs.[45] In the presence of N-doped $SrTiO_3$ nanoparticles, g-C_3N_4 exhibit much lower resistance than the pure g-C_3N_4 nanosheet which is evidenced by the drastically reduced diameter of the semicircle at the high-frequency region in the electrochemical impedance spectroscopy (EIS) patterns as shown in Fig. 8b. This result demonstrates that the g-C_3N_4/N-doped $SrTiO_3$ hetero/nanojunction can enhance the separation and transfer efficiency of photoinduced electron–hole pairs. This might be a favourable condition for improving the photocatalytic efficiency.

3.5 Photocurrent

The transient photocurrent responses of the CN and CNSTON samples were investigated to give further evidence to support the proposed photocatalytic mechanism. The photocurrent densities suddenly decrease to zero as soon as the lamp is turned off, and the photocurrent comes back to stable values when the lamp is turned on. This phenomenon indicates that the photoinduced electrons migrate to the ITO glass substrate to produce photocurrent under visible light irradiation.[46] As can be seen from Fig. 9, the hybrid nanocomposite shows higher photocurrent intensity than that of pure g-C_3N_4. The photoelectrochemical result also demonstrates a lower rate of recombination and high separation efficiency of photoinduced charge carriers for the g-C_3N_4/N-doped $SrTiO_3$ hybrid nanocomposites at the interface of the N-doped $SrTiO_3$ and g-C_3N_4. Therefore, the photoluminescence, electrochemical impedance and photocurrent results confirm the discussion on the charge carrier separation for improved photocatalytic performance (section 3.7.2).

3.6 Reusability

To test the stability and reusability of the prepared g-C_3N_4/N-doped $SrTiO_3$ nanocomposites, the successive experimental runs in the photocatalytic degradation of RhB in the presence

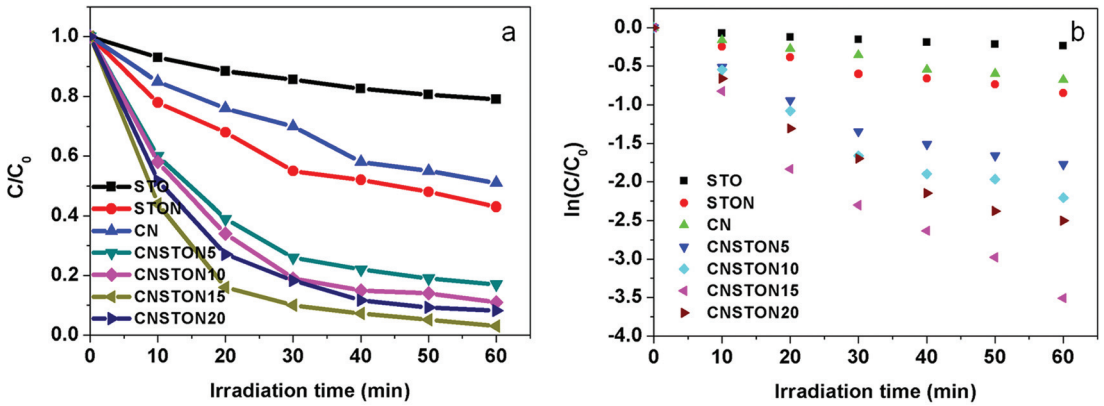

Fig. 7 Photocatalytic activity of the prepared photocatalysts for the degradation of RhB solution under visible light irradiation (a) and the $\ln(C/C_0)$ *vs.* time curves (b).

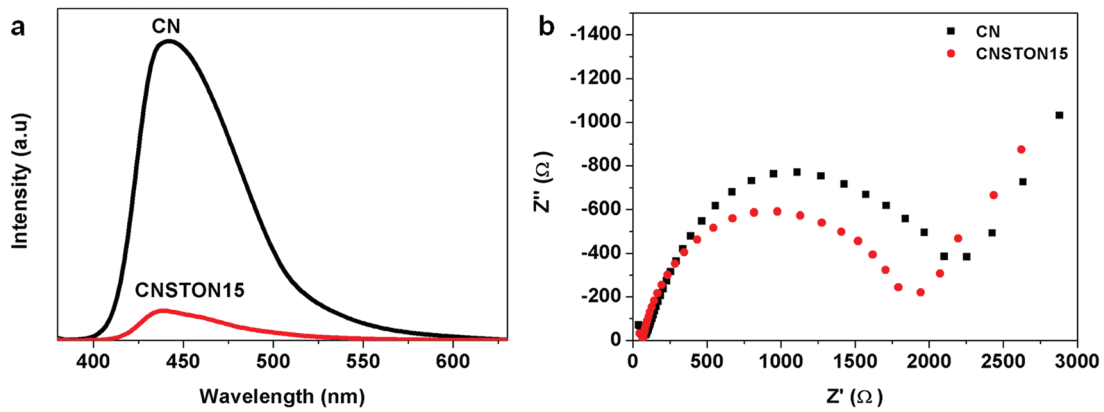

Fig. 8 Room temperature photoluminescence (excited at 365 nm) (a) and electrochemical impendence (b) spectra of CN and CNSTON15 photocatalysts.

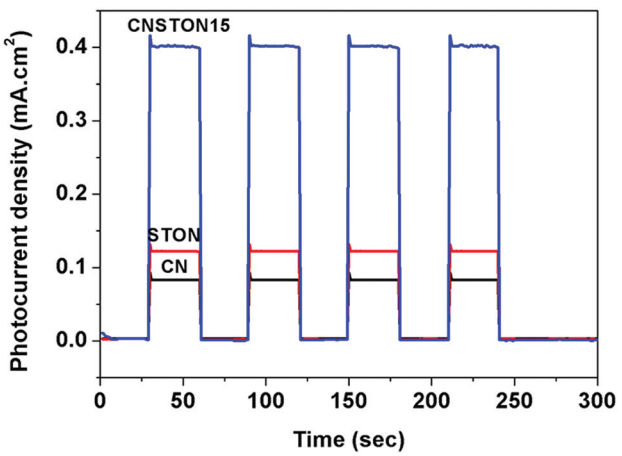

Fig. 9 Transient photocurrent response for the prepared photocatalysts with chopped visible light irradiation.

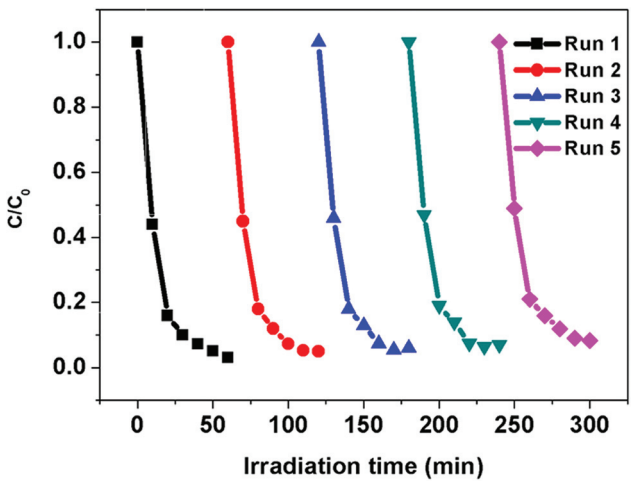

Fig. 10 Recyclability of the CNSTON15 photocatalyst for the degradation of RhB under visible light irradiation (five successive experimental runs).

of CNSTON15 under visible light irradiation were examined. It can be seen from Fig. 10 that the CNSTON15 photocatalyst still exhibited effective degradation of RhB even after five successive experimental runs and almost 90% photocatalytic efficiency was retained. Additionally, the XRD pattern of the reused CNSTON15 after the 5th cycle shown in Fig. S6† indicates that there is no change in phase and structure. Therefore,

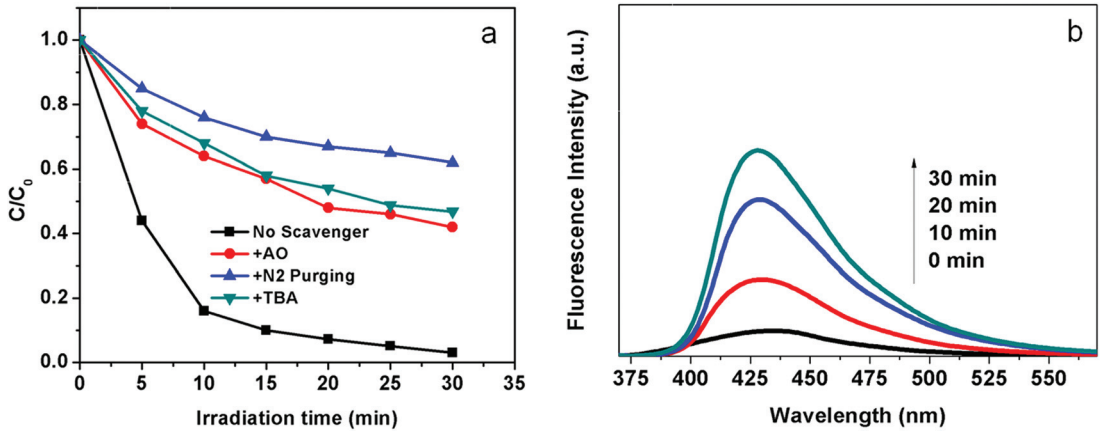

Fig. 11 (a) Effect of different scavengers on degradation of RhB in the presence of the CNNSTON15 photocatalyst under visible light irradiation. (b) ˙OH trapping PL spectra of the CNNSTON15 photocatalyst with TA solution under visible light irradiation.

the g-C_3N_4/N-doped $SrTiO_3$ hybrid nanocomposites possess high stability for photocatalytic oxidation of RhB under visible light irradiation and can be used as high-performance visible light photocatalysts in environmental protection.

3.7 Proposed photocatalytic mechanism

3.7.1 Role of reactive species. The roles of different scavengers such as ammonium oxalate (AO), tertiary butyl alcohol (TBA) and N_2 purging on the photocatalytic activity for degradation of RhB were investigated in an attempt to propose the possible mechanism. The AO, TBA and N_2 purging act as h^+, ˙OH, and $O_2^{\bullet-}$ scavengers, respectively.[28,40] As shown in Fig. 11a, the photocatalytic activity of the CNSTON15 was greatly suppressed by the addition of TBA as an ˙OH scavenger, indicating that ˙OH is an active species in the photocatalytic reaction. Meanwhile, a significant reduction in the photocatalytic efficiency was also observed by the addition of AO as an h^+ scavenger, as well as by conduction of N_2 purging as an $O_2^{\bullet-}$ scavenger. It is clear that $O_2^{\bullet-}$ and h^+ are also playing an almost equally important role in the photocatalytic degradation of RhB under visible light irradiation. Furthermore, during the photocatalytic reaction, the formation of ˙OH was confirmed by the photoluminescence spectra with TA as a probe molecule. As can be seen from Fig. 11b, the PL results indicate that the signal around 428 nm of 2-hydroxy terephthalic acid increases with the increase in irradiation time which is a measure of the formation of ˙OH on the surface of the photocatalyst.[47]

3.7.2 Proposed mechanism. Based on experimental results, a possible mechanism for photocatalytic degradation of RhB over the g-C_3N_4/N-doped $SrTiO_3$ hybrid nanocomposite was proposed. The high separation efficiency of the charge carrier may be due to the band structure matching between g-C_3N_4 and N-doped $SrTiO_3$. As can be seen from Fig. 12, the redox potentials of both the conduction band (−1.4 eV *vs.* NHE) and the valence band (+1.3 eV *vs.* NHE) of g-C_3N_4 are more negative than those of the conduction band (−0.2 eV *vs.* NHE) and the valence band (+3.0 eV *vs.* NHE) of $SrTiO_3$.[30,48]

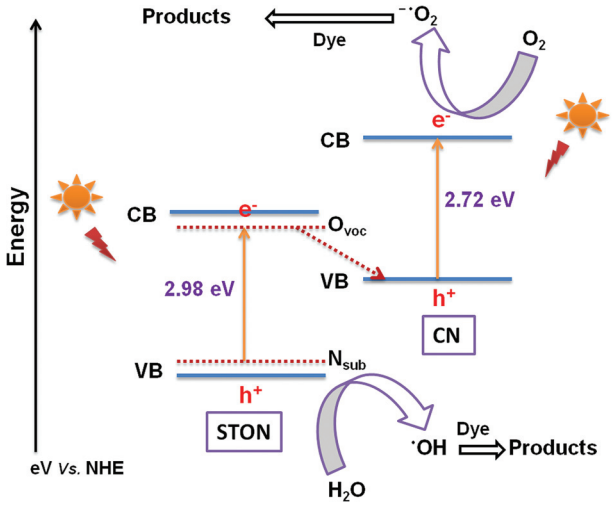

Fig. 12 Schematic diagram of the mechanism for high separation efficiency of photoinduced charge carrier and transfer in the g-C_3N_4/N-doped $SrTiO_3$ system under visible light irradiation.

Under visible light, the photoinduced electrons with low reductive power in the CB of STON transfer to the VB of CN quickly, resulting in the combination of these electrons with photoinduced holes with low oxidative power of CN, and accumulated rich electrons with high reductive power in the CB of CN and holes with high reductive power in the VB of STON which can participate efficiently in the reduction and oxidation reactions, respectively. This is because the electrons in the CB of N-doped $SrTiO_3$ cannot produce $O_2^{\bullet-}$ from dissolved O_2 by the photoreduction process as the conduction edge potential (−0.2 eV *vs.* NHE) is more positive than the standard redox potential $E^0_{(O_2/O_2^{\bullet-})}$ (−0.3 eV *vs.* NHE). Whereas the photoinduced holes of g-C_3N_4 also cannot oxidize the adsorbed H_2O molecules to ˙OH as the valance edge potential (+1.3 eV *vs.* NHE) is more negative than standard redox potential $E^0_{(\bullet OH/H_2O)}$ (+2.8 eV *vs.* NHE), suggesting that the charge carrier transfer in accordance with the most common model (*i.e.* transfer of electrons from CB of CN to CB of STON) is not

favorable for the generation of the main reactive species $O_2^{\bullet-}$ and $^{\bullet}OH$.[49] According to Fig. 12, the electrons in the CB of CN have more negative potential to reduce the molecular oxygen to yield $O_2^{\bullet-}$. The holes in the valance band of STON have more positive potential to generate abundant active $^{\bullet}OH$ for effective oxidation. Therefore, the photocatalytic activity can be significantly improved due to high separation efficiency of charge carriers in the g-C_3N_4/N-doped $SrTiO_3$ hybrid system. According to the results, a direct Z-scheme mechanism was proposed for the real separation process of photoinduced electron–hole pairs. Hence, the g-C_3N_4/N-doped $SrTiO_3$ system is a type of direct Z-scheme photocatalyst under visible light irradiation.

4. Conclusion

Novel g-C_3N_4/N-doped $SrTiO_3$ hybrid nanocomposites with improved photocatalytic performance under visible light were successfully prepared. The results clearly indicated that the N-doped $SrTiO_3$ nanoparticles successfully wrapped in the layers of g-C_3N_4 nanosheets. The special structure is believed to be beneficial for charge separations. The hybrid nanocomposites exhibited an improved photocurrent response under visible light irradiation. The optimum photocatalytic activity of g-C_3N_4/N-doped $SrTiO_3$ at 15 wt% of N-doped $SrTiO_3$ is much higher than that of pure g-C_3N_4 and N-doped $SrTiO_3$ under visible light. The PL spectra indicate that the formation of g-C_3N_4/N-doped $SrTiO_3$ heterostructures decreases the recombination of photoinduced electron–hole pairs. These results indicate that the improved photocatalytic efficiency is mainly due to high charge separation efficiency and band energy matching and the decreased recombination for g-C_3N_4/N-doped $SrTiO_3$ hetero/nanojunction. Therefore, these hybrid nanocomposites are a promising candidate for degradation of organic pollutants under visible light.

Acknowledgements

The corresponding author thanks the Department of Science and Technology, Government of India for providing financial support under young scientist scheme (SR/FT/CS-096/2009). Santosh Kumar thanks the Ministry of Human Resource Development, Government of India for providing Research fellowship.

References

1 M. R. Hoffmann, S. T. Martin, W. Choi and D. W. Bahnemann, *Chem. Rev.*, 1995, **95**, 69.
2 V. K. Prashant, *J. Phys. Chem. C*, 2007, **111**, 2834.
3 X. Chen, S. Shen, G. Liejin and S. M. Samuel, *Chem. Rev.*, 2010, **110**, 6503.
4 Y. Qu and X. Duan, *Chem. Soc. Rev.*, 2013, **42**, 2568.
5 K. Rajeshwar, M. E. Osugi, W. Chanmanee, C. R. Chenthamarakshan, M. V. B. Zanoni, P. Kajitvichyanukul and R. Krishnan-Ayer, *J. Photochem. Photobiol., C*, 2008, **9**, 171.
6 A. Fujishima and K. Honda, *Nature*, 1972, **238**, 37.
7 J. Zhao and X. D. Yang, *Build. Environ.*, 2003, **38**, 645.
8 T. K. Townsend, N. D. Browning and F. E. Osterloh, *ACS Nano*, 2012, **6**, 7420.
9 A. Kudo and H. Kato, *Chem. Phys. Lett.*, 2000, **331**, 373.
10 H. Zhou, Y. Qu, T. Zeid and X. Duan, *Energy Environ. Sci.*, 2012, **5**, 6732.
11 S. Y. Lee and S. J. Park, *J. Ind. Eng. Chem.*, 2013, **19**, 1761.
12 Y. Wang, Q. Wang, X. Zhan, F. Wang, M. Safdar and J. He, *Nanoscale*, 2013, **5**, 8326.
13 R. M. Mohamed, D. L. McKinney and W. M. Sigmund, *Mater. Sci. Eng., R*, 2012, **73**, 1.
14 X. Wang, K. Maeda, A. Thomas, K. Takanabe, X. Gang, J. M. Carlsson, K. Domenm and M. Antonietti, *Nat. Mater.*, 2009, **8**, 76.
15 P. Niu, L. Zhang, G. Liu and H. M. Cheng, *Adv. Funct. Mater.*, 2012, **22**, 4763.
16 F. T. Wagner and G. A. Somorjai, *Nature*, 1980, **285**, 559.
17 Y. Xu and M. A. A. Schoonen, *Am. Mineral.*, 2000, **85**, 543.
18 K. Iizuka, T. Wato, Y. Miseki, K. Saito and A. Kudo, *J. Am. Chem. Soc.*, 2011, **133**, 20863.
19 Z. Jiang, T. Xiao, V. L. Kuznetsov and P. P. Edwards, *Philos. Trans. R. Soc. London, Ser. A*, 2010, **368**, 3343.
20 Y. Y. Mi, Z. Yu, S. J. Wang, X. Y. Gao, A. T. S. Wee, C. K. Ong and C. H. A. Huan, *J. Appl. Phys.*, 2007, **101**, 063708.
21 S. Ouyang, H. Tong, N. Umezawa, J. Cao, P. Li, Y. Bi, Y. Zhang and J. Ye, *J. Am. Chem. Soc.*, 2012, **134**, 1974.
22 R. Asahi, T. Morikawa, T. Ohwaki, K. Aoki and Y. Taga, *Science*, 2001, **293**, 269.
23 J. Liu, L. Wang, J. Liu, T. Wang, W. Qu and Z. Li, *Cent. Eur. J. Phys.*, 2009, **7**, 762.
24 J. Wang, H. Li, H. Li, S. Yin and T. Sato, *Solid State Sci.*, 2009, **11**, 182.
25 J. Wang, S. Yin, M. Komatsu, Q. Zhang, F. Saito and T. Sato, *J. Photochem. Photobiol., A*, 2004, **165**, 149.
26 Z. Zhang, G. Liu and Y. Mao, *Int. J. Hydrogen Energy*, 2013, **38**, 9349.
27 Y. Wang, R. Shi, J. Lin and Y. Zhu, *Energy Environ. Sci.*, 2011, **4**, 2922.
28 S. Kumar, T. Surendar, A. Baruah and V. Shanker, *J. Mater. Chem. A*, 2013, **1**, 5333.
29 X. Xu, G. Liu, C. Randorn and J. T. S. Irvine, *Int. J. Hydrogen Energy*, 2011, **36**, 13501.
30 H. W. Kang, S. N. Lim, D. Song and S. B. Park, *Int. J. Hydrogen Energy*, 2012, **37**, 11602.
31 S. Chen, L. Ji, W. Tang and X. Fu, *Dalton Trans.*, 2013, **42**, 10759.
32 H. J. Yun, H. Lee, N. D. Kim, D. M. Lee, S. Yu and J. Yi, *ACS Nano*, 2011, **5**, 4084.
33 N. Fu, Z. Jin, Y. Wu, G. Lu and D. Li, *J. Phys. Chem. C*, 2011, **115**, 8586.
34 L. Xu, E. M. P. Steinmiller and S. E. Skrabalak, *J. Phys. Chem. C*, 2012, **116**, 871.

35 Z. Xu, S. Chenghua, Y. Hua, G. C. Zhi, X. Zheng, Y. Delai, Q. L. Gao, L. Xinyong and W. Lianzhou, *J. Phys. Chem. C*, 2013, **117**, 4937.
36 J. W. Wang, W. Zhu, Y. Q. Zhang and S. X. Liu, *J. Phys. Chem. C*, 2007, **111**, 1010.
37 S. Sakthivel, M. Janczarek and H. Kisch, *J. Phys. Chem. B*, 2004, **108**, 19384.
38 J. H. Yan, Y. R. Zhu, Y. G. Tang and S. Q. Zheng, *J. Alloys Compd.*, 2009, **472**, 429.
39 J. X. Sun, Y. P. Yuan, L. G. Qiu, X. Jiang, A. J. Xie, Y. H. Shen and J. F. Zhu, *Dalton Trans.*, 2012, **41**, 6756.
40 Y. Li, J. Wang, H. Yao, L. Dang and Z. Li, *J. Mol. Catal. A: Chem.*, 2011, **334**, 116.
41 S. Kumar, T. Surendar, B. Kumar, A. Baruah and V. Shanker, *J. Phys. Chem. C*, 2013, **117**, 26135.
42 S. Sato, *Chem. Phys. Lett.*, 1986, **123**, 126.
43 X. B. Chen and C. Burda, *J. Phys. Chem. B*, 2004, **108**, 15446.
44 L. Jing, Y. Qu, B. Wang, S. Li, B. Jiang, L. Yang, W. Fu, H. Fu and J. Sun, *Sol. Energy Mater. Sol. Cells*, 2006, **90**, 1773.
45 H. Zhang, X. Lv, Y. Li, Y. Wang and J. Li, *ACS Nano*, 2010, **4**, 380.
46 J. G. Yu, G. P. Dai and B. Cheng, *J. Phys. Chem. C*, 2010, **114**, 19378.
47 K. Ishibashi, A. Fujishima, T. Watanabe and K. Hashimoto, *Electrochem. Commun.*, 2000, **2**, 207.
48 H. Ji, F. Chang, X. Hua, W. Qin and J. Shen, *Chem. Eng. J.*, 2013, **218**, 183.
49 S. Kumar, A. Baruah, T. Surendar, B. Kumar, V. Shanker and B. Sreedhar, *Nanoscale*, 2014, **6**, 4830.